ADVANCED MATERIALS
www.advmat.de

www.MaterialsViews.com

Theory of Sliding-Mode Triboelectric Nanogenerators

*Simiao Niu, Ying Liu, Sihong Wang, Long Lin, Yu Sheng Zhou, Youfan Hu, and Zhong Lin Wang**

The triboelectric nanogenerator (TENG) is a powerful approach toward new energy technology, especially for portable electronics. A theoretical model for the sliding-mode TENG is presented in this work. The finite element method was utilized to characterize the distributions of electric potential, electric field, and charges on the metal electrodes of the TENG. Based on the FEM calculation, the semi-analytical results from the interpolation method and the analytical *V-Q-x* relationship are built to study the sliding-mode TENG. The analytical *V-Q-x* equation is validated through comparison with the semi-analytical results. Furthermore, based on the analytical *V-Q-x* equation, dynamic output performance of sliding-mode TENG is calculated with arbitrary load resistance, and good agreement with experimental data is achieved. The theory presented here is a milestone work for in-depth understanding of the working mechanism of the sliding-mode TENG, and provides a theoretical basis for further enhancement of the sliding-mode TENG for both energy scavenging and self-powered sensor applications.

1. Introduction

With the rapid growth of the worldwide energy demand, scavenging energy from the ambient environment is of great importance in modern society.[1–4] Among all types of energy sources, mechanical energy, such as friction and vibration energy, is attracting more and more attention due to the fact that it is clean and universally available. Compared to other mechanical energy harvesting techniques,[5–7] the triboelectric nanogenerator (TENG) has the following advantages: its high output power, high efficiency, cost-effective materials, and convenient fabrication.[8–13] The working principle of the TENG is based on the coupling of the triboelectric effect[14,15] and the electrostatic induction. The TENGs have two basic working modes: the contact-mode[8–10] and the sliding-mode.[11–13] Compared to the contact-mode, the sliding-mode is much easier for packaging and more effective for static charge generation. Although the basic design and device structures of the sliding-mode TENG have been demonstrated, a systematic theoretical model for this working mode has not been developed yet.

The kernel part of the theory for TENG is the relationship among three parameters: 1) its output voltage (V), 2) the amount of charge transferred between electrodes (Q), and 3) the separation distance (x) (V-Q-x relationship). This relationship is similar to the linear V-Q relationship for a capacitor. However, because of the non-uniform charge distribution on the surface of the metal electrodes, the V-Q-x relationship of a sliding-mode TENG is highly complicated. Therefore, it is difficult to construct an accurate analytical V-Q-x relationship. To address this problem, we utilized numerical calculation methods such as the finite element method (FEM) to calculate the electric potential distribution in the dielectrics and charge distribution on the electrodes. Based on the numerical calculated results, a semi-analytical and an analytical V-Q-x relationship were constructed through the interpolation method. Finally, based on the approximate analytical V-Q-x equation, we calculated the theoretical output of a TENG and compared it with experimental data to verify its validity.

2. Dielectric-to-Dielectric Sliding-Mode TENG

Considering the materials to be used as the pair of the triboelectric layers, the sliding-mode TENG has two types: dielectric-to-dielectric and conductor-to-dielectric. We first take the dielectric-to-dielectric category as an example. The model for this type of TENG was built with dimensions close to those of the real device, as shown in **Figure 1**a. Considering that the width w of the whole structure (10 cm) is much larger than the thickness (0.22 mm), a 2D model was utilized to simplify the calculation. The geometric size of the two dielectrics was 10 cm in longitudinal direction (represented by l) and 0.22 mm in thickness direction (represented by d_1 and d_2). Two metal electrodes with a thickness of 0.01 mm were bonded with the two dielectrics layers. The bottom part was fixed while the top could slide through the longitudinal direction. The lateral separation distance was defined as x. When the two dielectrics were separated, the lower surface of Dielectric 1 and the upper surface of Dielectric 2 had charges with different signs at the non-overlapped regions, which are because of the triboelectric effect.[16] Due to the nature of this effect, it is reasonable to assume that those triboelectric charges (tribo-charges) are uniformly

S. Niu, Y. Liu, S. Wang, L. Lin, Y. S. Zhou,
Dr. Y. Hu, Prof. Z. L. Wang
School of Materials Science and Engineering
Georgia Institute of Technology
Atlanta, GA, 30332–0245, USA
Prof. Z. L. Wang
Beijing Institute of Nanoenergy and Nanosystems
Chinese Academy of Sciences
Beijing, China
E-mail: zhong.wang@mse.gatech.edu

DOI: 10.1002/adma.201302808

distributed on these two surfaces, which is an excellent approximation for insulators. Also, the decay of tribo-charges with time can be neglected on these insulating polymers.[17] The overall density of tribo-charges on the overlapped surface can be regarded as 0 because the distance between the center of the positive charges and the negative charges are in atomic level. The surface density of the tribo-charges is defined as σ (7 μC m^{-2}) at surface of Dielectric 1 and -σ at surface of Dielectric 2. This entire structure is surrounded by air, as the usual case in experiments. The potential at infinity is chosen as the reference point for electric potential, which is 0.

The FEM calculation under the open-circuit (OC) condition of the above structure was carried out utilizing the COMSOL software. To apply the OC boundary condition, the total surface charge density at each metal electrode was assigned as 0. The electric potential distributions with variable separation distances are shown in Figure 1b. The mesh convergence of the output voltage at 5-cm separation condition is shown in Figure 1c to validate the FEM calculation results. The electric potential of the top electrode is positive while that of the bottom electrode is negative due to the electrostatic induction of the tribo-charges. With the increase of x, the open-circuit electric potential difference (V_{OC}) between these two electrodes also increases. Furthermore, the slope of the V_{OC}-x curve is getting much higher when x is approaching to l. The detailed plot of V_{OC}-x relationship is shown in Figure 1d. Figure 1e and f show the distributions of electric field in X and Y-direction. Strong X-component of electric field only exists at the edge of the two dielectrics. Inside the dielectrics, the electric field mainly has a large Y-direction component, which is nearly uniform except the edge regions where the edge effect should be considered. It could also be found that the Y-direction component is positive in the non-overlapped regions while negative in the overlapped regions. When the edge effect can be neglected, the nearly uniform Y-direction electric field leads to uniform charge distributions on the metal electrodes at each region, as shown in Figure 1g and h. Take the bottom electrode as an example, at the non-overlapped regions, the charge density is approximately 7 μC m^{-2}, which equals to the opposite number of the surface density of tribo-charges of Dielectric 2. While at the overlapped regions, the uniform negative charges are present, which is because the total charges in each electrode are 0 at the OC condition. At the edges of each region, the charge distribution is no longer uniform and peaks will exist at the two ends of the dielectrics, which is still due to the edge effect. The peaks are much higher when x = 9 cm, as shown in the inset of Figure 1g and h, which means that the edge effect is much more severe when x approaches to l.

To further understand the behavior of the TENG, FEM model at the short-circuit (SC) condition was calculated, as shown in **Figure 2**. To apply the SC boundary condition, the two electrodes were assigned as the same electric potential. In addition, to maintain charge equilibrium, the summation of the charges at the two electrodes was assigned as 0. The electric field distributions of both X-direction and Y-direction are shown in Figure 2a and b. Similar to the case in the OC condition, the strong X-direction component of the electric field only exists at the edge of the dielectrics. Inside the dielectrics, the electric field has mainly Y-direction component. At the separated

Simiao Niu is a Ph.D. candidate working as a graduate research assistant in the School of Material Science and Engineering at the Georgia Institute of Technology, under the supervision of Dr. Zhong Lin Wang. He earned his B.E. degree in Institute of Microelectronics at Tsinghua University in 2011. His doctoral research interests include theoretical and experimental studies on: mechanical energy harvesting by triboelectric nanogenerators and high-performance piezotronic and piezo-phototronic sensors based on piezoelectric nanowires.

Ying Liu received her B.S. in physics from the Yuanpei program at Peking University in 2009 and is a Ph.D. candidate with Prof. Zhong Lin Wang in the School of Materials Science and Engineering at the Georgia institute of Technology. Her main research interest is the coupling of mechanics, electronics, and photonics in the same material, which includes piezo-phototronics and triboelectrics.

Dr. Zhong Lin Wang is a Hightower Chair and Regents's Professor at Georgia Tech. He is also the Chief scientist and Director for the Beijing Institute of Nanoenergy and Nanosystems, Chinese Academy of Sciences. His discovery and breakthroughs in developing nanogenerators establish the principle and technological road map for harvesting mechanical energy from environment and biological systems for powering personal electronics. His research on self-powered nanosystems has inspired the worldwide effort in academia and industry for studying energy for micro-nano-systems, which is now a distinct disciplinary in energy research and future sensor networks. He coined and pioneered the field of piezotronics and piezo-phototronics by introducing piezoelectric potential gated charge transport process in fabricating new electronic and optoelectronic devices. This historical breakthrough by redesign CMOS transistor has important applications in smart MEMS/NEMS, nanorobotics, human-electronics interface and sensors.

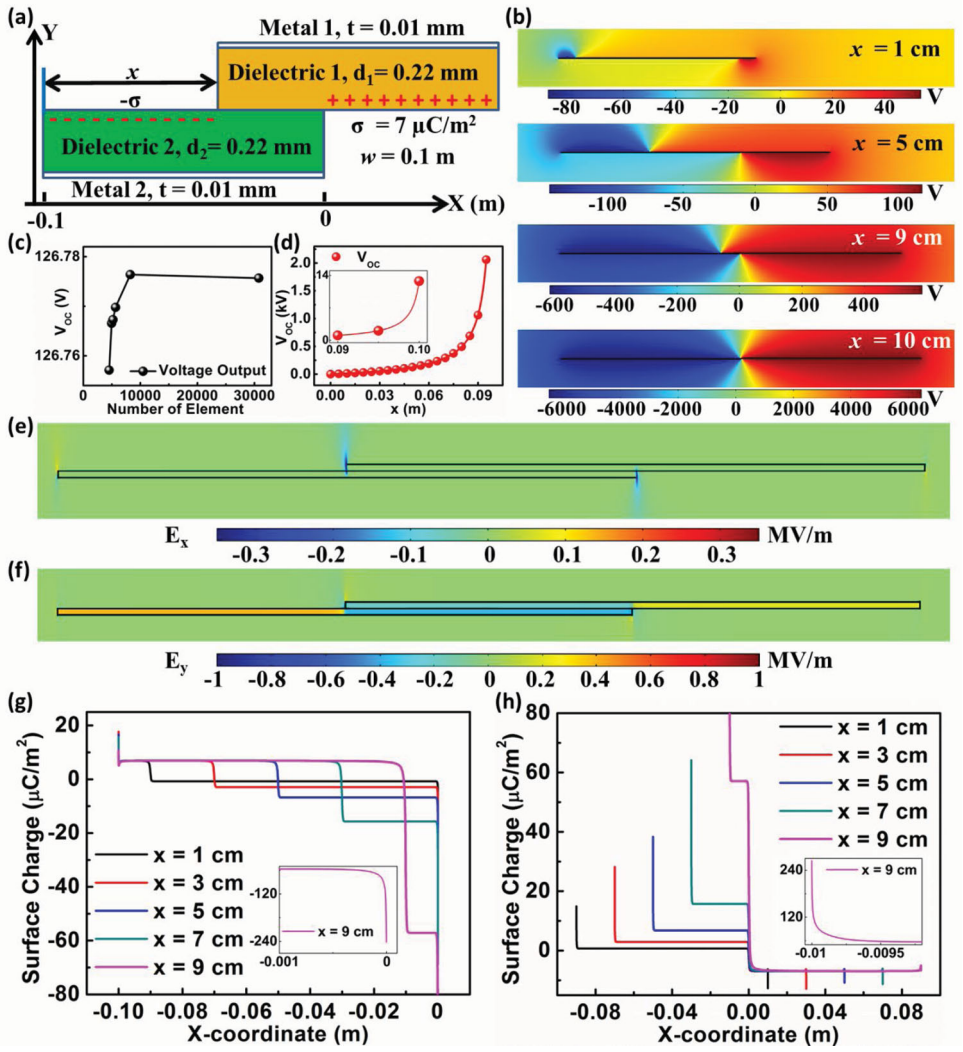

Figure 1. FEM calculation results of dielectric-to-dielectric TENG in open-circuit (OC) condition. (a) Structure of the FEM model. (b) Calculated electric potential distributions at different sliding distances *x*. (c) Mesh convergence of V_{OC} when x = 5 cm. (d) Calculated V_{OC} at different *x*, the inset is the profile of the V_{OC} when *x* approaches to *l*. (e,f) Distribution of (e) the X-component and (f) the Y-component of the electric field (the scale in X-direction is 1:5 to the real case). (g,h) Calculated charge distribution of (g) the upper face of the bottom electrode and (h) the lower face of the top electrode, the inset is the enlarged profile of the surface charges at the edges when x = 0.09 m.

regions, the electric field is uniform and along the positive Y-direction. However, unlike the case in the OC condition, the Y-component is nearly 0 at the overlapped regions. This is because in the SC condition, there is no electric potential difference between the two electrodes. This electric field distribution corresponds to a specific charge distribution of the two electrodes, as shown in Figure 2c and d. Take the bottom electrode as an example, at the non-overlapped regions, the charge density is close to 7 μC m^{-2}, similar to the case in the OC condition. However, because net electrons are transferred from the bottom electrode to the top electrode, the charge density is approximately 0 at the overlapped regions. The amount of the charges at each individual electrode is the same but with opposite signs. Through the integration of the charges at bottom electrode, the total amount of transferred charge at SC condition (Q_{SC}) is calculated and its relationship with *x* is shown in Figure 2e. Q_{SC} has an approximately linear relationship with *x* when the two dielectrics are not completely separated.

The FEM calculation above shows that the voltage output of TENG (*V*) has a specific relationship with both the total amount of transferred charges between electrodes (*Q*) and the separation distance *x*. To analyze this relationship, voltage output of TENG (*V*) at different *Q* and different *x* is calculated. The *V*-*Q* relationship at different *x* is shown in **Figure 3**a. Similar to a traditional capacitor, at a constant *x*, the voltage output *V* and the total charge *Q* show a remarkably accurate linear relationship. However, unlike a capacitor, the intercept is not 0. The linear *V*-*Q* relationship is due to the capacitance formed between the two electrodes and the non-zero intercept results from the tribo-charges at the surface of the two dielectrics. From the linear relationship, Equation (1) can be utilized to express the *V*-*Q*-*x* relationship of the TENG,

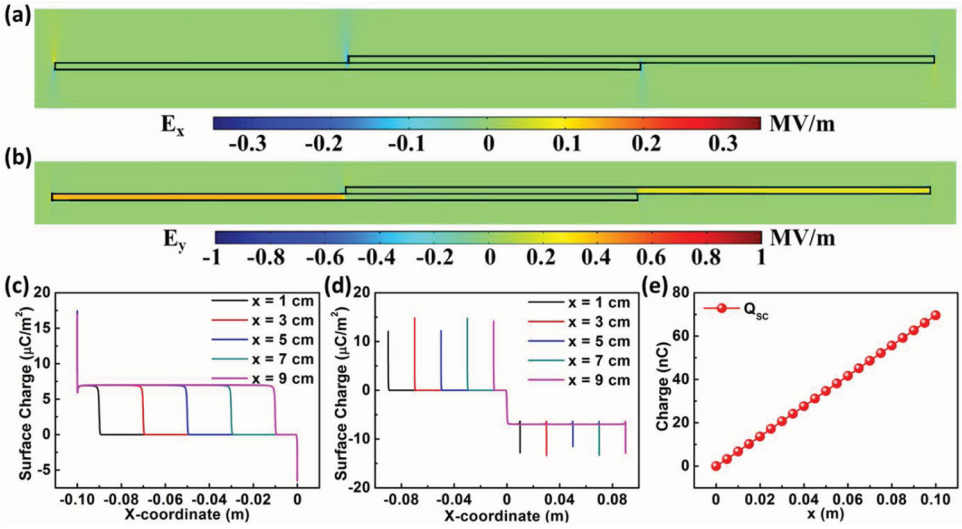

Figure 2. FEM calculation results of dielectric-to-dielectric TENG in short-circuit (SC) condition. (a-b) Distributions of (a) the X-component and (b) the Y-component of the electric field (the scale in X-direction is 1:5 to the real case). (c-d) Calculated charge distributions on (c) the upper face of the bottom electrode and (d) the lower face of the top electrode. (e) Calculated Q_{SC} at different *x*.

$$V = -A(x) \times Q + B(x) \tag{1}$$

The physical meaning of the parameter *A* is the reciprocal value of the capacitance *C* formed between the two electrodes and the physical meaning of parameter *B* is the voltage output when *Q* equals to 0, which is the open circuit voltage (V_{OC}). Therefore, Equation (1) can be rewritten as:

$$V = -\frac{1}{C(x)} \times Q + V_{OC}(x) \tag{2}$$

The dependences of both parameters (*A* and *B*) with different *x* are extracted by the interpolation method, which are listed in the Table S1, Supporting Information and plotted in Figure 3b and c. To obtain the final semi-analytical equation, a second-time interpolation was utilized to extract the *A*-*x* and *B*-*x* relationships. Noting that the slopes of *A*-*x* and *B*-*x* relationships are fairly large when *x* approaches *l*, continuous fraction interpolation is utilized to better characterize these relationships instead of traditional polynomial interpolation.[18] The standard continuous fraction interpolation equation is shown as Equation (3).[18] The values of the interpolation parameters are listed in Table S2.

$$A(x) = a_1 + \frac{x - x_1}{a_2 + \frac{x - x_2}{a_3 + \cdots + \frac{x - x_{10}}{a_{11}}}} \tag{3a}$$

$$B(x) = b_1 + \frac{x - x_1}{b_2 + \frac{x - x_2}{b_3 + \cdots + \frac{x - x_{10}}{b_{11}}}} \tag{3b}$$

The interpolation results of parameters *A* and *B* are plotted in the Figure 3b and c. These interpolation results are accurate and have little error. The semi-analytical *V*-*Q*-*x* relationship can be obtained by merging Equation (3) into Equation (1). However, to understand the physics under the sliding-mode TENG, an analytical equation rather than the semi-analytical

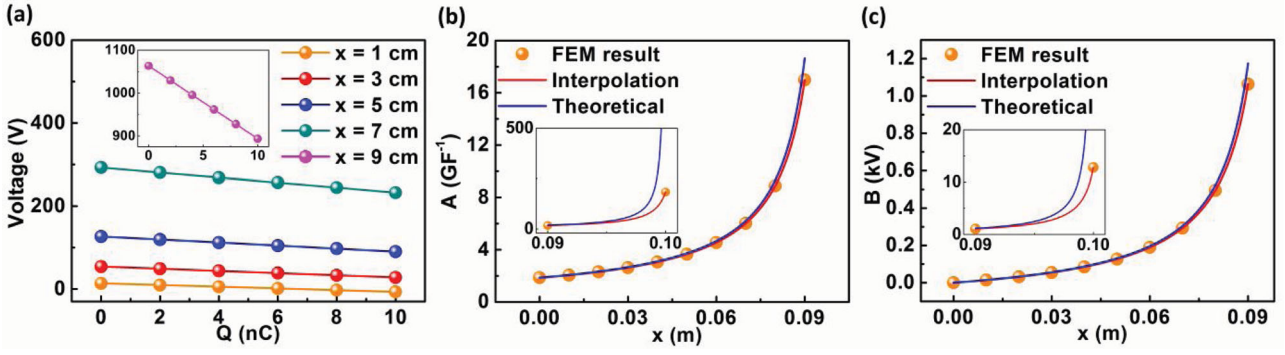

Figure 3. Analysis of the *V*-*Q*-*x* relationship. (a) FEM-calculated linear *V*-*Q* relationship of dielectric-on-dielectric TENG. (b-c) Comparisons of parameters (b) *A* and (c) *B* obtained through different methods: numerical FEM calculation, semi-analytical interpolation, and theoretical equation. The insets are the profile of the parameters (b) *A* and (c) *B* when *x* approaches to *l*.

equation is preferred. Although it is difficult to derive the accurate analytical equation, utilizing the results of Equation (2) and some approximations, an approximate analytical equation was obtained by deriving the capacitance C between the two electrodes and the open circuit voltage V_{OC} in Equation (2).

The capacitance C is first deducted. Since the thickness of the dielectrics is much smaller than their length, the capacitor between the overlapped region is the dominate part of the total capacitance as long as the two dielectrics are not close to thoroughly separated. Therefore, utilizing the parallel-plate capacitor model, the total capacitance C can be estimated by the following equation:

$$C = \frac{\varepsilon_0 w (l - x)}{\frac{d_1}{\varepsilon_{r1}} + \frac{d_2}{\varepsilon_{r2}}} \quad (4)$$

where the ε_{r1} and ε_{r2} represent the relative permittivity of Dielectric 1 and Dielectric 2.

V_{OC} can be estimated by utilizing the charge distribution calculated by FEM in Figure 1g and h. Since the length of the dielectrics is much larger than the thickness, we can assume in each region, the metal electrodes work as infinite plates. Under this approximation, the charge distribution is uniform in each region, and the electric field is uniform along the Y-direction inside the dielectrics. Therefore, in an ideal case, the absolute value of surface charge density is σ for the non-overlapped region. For the overlapped region, the charge density is still uniform. Thus, if the charges at the outer side of the electrode can be neglected, the charge density at the overlapped region can be calculated through the 0 total charges at each electrode at OC condition. The ideal charge distribution at OC condition can be approximated by the following equations:

$$\text{For the non-overlapped region of the bottom electrode : } \rho = \sigma \quad (5a)$$

$$\text{For the overlapped region of the bottom electrode : } \rho = -\frac{\sigma x}{l - x} \quad (5b)$$

$$\text{For the non-overlapped region of the top electrode : } \rho = -\sigma \quad (5c)$$

$$\text{For the overlapped region of the top electrode : } \rho = \frac{\sigma x}{l - x} \quad (5d)$$

Utilizing the charge distribution shown above and Gauss Theorem, the electric field of the overlapped region in Dielectric 1 and Dielectric 2 E_{y1} and E_{y2} can be given by:

$$E_{y1} = \frac{\sigma x}{\varepsilon_0 \varepsilon_{r1} (l - x)} \quad (6a)$$

$$E_{y2} = \frac{\sigma x}{\varepsilon_0 \varepsilon_{r2} (l - x)} \quad (6b)$$

E_{y1} and E_{y2} are along the negative Y-direction.
Thus, the V_{OC} is given by:

$$V_{OC} = E_{y1} d_1 + E_{y2} d_2 = \frac{\sigma x}{\varepsilon_0 (l - x)} \left(\frac{d_1}{\varepsilon_{r1}} + \frac{d_2}{\varepsilon_{r2}} \right) \quad (7)$$

Substituting Equation (7) and Equation (4) into Equation (2), the approximate V-Q-x relationship of the sliding TENG can be given by:

$$V = -A \times Q + B = -\frac{1}{w \varepsilon_0 (l - x)} \left(\frac{d_1}{\varepsilon_{r1}} + \frac{d_2}{\varepsilon_{r2}} \right) Q + \frac{\sigma x}{\varepsilon_0 (l - x)} \left(\frac{d_1}{\varepsilon_{r1}} + \frac{d_2}{\varepsilon_{r2}} \right) \quad (8)$$

The parameters A and B estimated by Equation (8) are also plotted in Figure 3b and c for comparison. When x is less than 8 cm, the estimated result by Equation (8) accurately matches the FEM calculation results and the interpolation results. However, when x approaches to l, the parameters estimated by Equation (8) approach to infinity and the error is significant. This error origins from the assumption of Equation (8), that the edge effect can be neglected, which is satisfied under both of the following two conditions. First, the aspect ratio of the geometry must be sufficiently large, in other words, the length l must be significantly larger than the thickness d_1 and d_2. Otherwise, the Y-component of the electric field inside the dielectrics will not be uniform and additional X-component of electric field will exist inside the dielectrics. Both of them will lead to non-uniform charge distributions at the metal electrodes. This non-ideal effect is shown in Figure S1, where the aspect ratio is only 10. However, in practical sliding TENG experiments, the length l is usually larger than 3 cm and the thickness is around 0.1 mm. Therefore, this non-ideal effect can be neglected in real applications. Second, the separation distance x should not be close to the length of dielectrics l. Three non-ideal factors will take effect when x gets close to l. First, when x is close to l, the capacitance of the separated region can rival to the parallel-plate capacitance because the overlapped region is too narrow. Thus, the estimation of C by Equation (4) will have a significant error. In addition, when x approaches to l, as shown in Figure 1g and h, at OC condition, the charge density at the edges will be sufficiently high and cannot be neglected. Thus, when the zero-charge condition is utilized to calculate the charge density in the overlapped regions, the theoretical results will deviate from the FEM calculation result. For instance, when x = 9 cm, for the overlapped region at the bottom electrode, the charge density estimated by Equation (5b) is –63 μC m^{-2}, while the charge density from FEM calculation is only –57.07 μC m^{-2} with about 10% deviation. Finally, when x is close to l, the charges at the upper surface of metal 1 and the lower surface of metal 2 cannot be neglected. This also results in inaccurate estimation of the surface charge density. Although this factor can affect the accuracy of Equation (8), such influence will get severe only when x is larger than 0.9l, which is a very small region. Furthermore, in such a small region, it contributes very little to overall total charge transfer. Therefore, the Equation (8) is an accurate estimation in most cases in application.

The output performance of a TENG at the OC and SC working conditions can be estimated from the above equations. At the OC condition, the V_{OC} can be estimated by Equation (7). At the SC condition, the amount of transferred charge Q_{SC} can also be estimated by putting $V = 0$ into the Equation (8). Therefore, the Q_{SC} is given by:

$$Q_{SC} = \sigma w x \quad (9)$$

This equation explains the TENG behavior shown in Figure 2e. From this equation, the short circuit current is given by:

$$I_{SC} = \sigma w \frac{dx}{dt} = \sigma w v(t) \tag{10}$$

More generally, when a sliding TENG is connected with an arbitrary resistor R, the output performance can be estimated by the combination with the kernel equation for sliding TENG Equation (8) and basic I–V relationship of a resistor. For a resistor, the current I and voltage V follows the Ohm's law:

$$V = I R = R\frac{dQ}{dt} \tag{11}$$

Merge Equation (11) into Equation (8), we can get that

$$R\frac{dQ}{dt} = -\frac{1}{w\varepsilon_0 (l-x)}\left(\frac{d_1}{\varepsilon_{r1}} + \frac{d_2}{\varepsilon_{r2}}\right)Q + \frac{\sigma x}{\varepsilon_0 (l-x)}\left(\frac{d_1}{\varepsilon_{r1}} + \frac{d_2}{\varepsilon_{r2}}\right) \tag{12}$$

Equation (12) is a first-order ordinary differential equation. Considering that $x\ (t = 0) = 0$, the boundary condition is $Q\ (t = 0) = 0$. With this boundary condition, Equation (12) can be utilized to numerically calculate the Q, I and V for an arbitrary motion process. For some special motion processes, such as moving at a constant speed v, Equation (12) can be analytically solved, and the results are given below. (d_0 is a thickness constant defined as $\frac{d_1}{\varepsilon_{r1}} + \frac{d_2}{\varepsilon_{r2}}$)

$$Q = \sigma l w\left\{-\frac{Rw\varepsilon_0 v}{Rw\varepsilon_0 v - d_0}\exp\left[\frac{d_0}{Rw\varepsilon_0 v}\ln\left(\frac{l-vt}{l}\right)\right] + \frac{d_0}{Rw\varepsilon_0 v - d_0}\left(1 - \frac{vt}{l}\right) + 1\right\} \tag{13a}$$

for $Rw\varepsilon_0 v \neq d_0$ and $t < l/v$

$$Q = \sigma w \times \left[vt + (l - vt)ln\left(1 - \frac{vt}{l}\right)\right] \tag{13b}$$

for $Rw\varepsilon_0 v = d_0$ and $t < l/v$

The current I is derived from the differentiation of Q by t:

$$I = \sigma w v \frac{d_0}{Rw\varepsilon_0 v - d_0}\left\{\frac{l}{l - vt}\exp\left[\frac{d_0}{Rw\varepsilon_0 v}\ln\left(\frac{l-vt}{l}\right)\right] - 1\right\} \tag{14a}$$

when $Rw\varepsilon_0 v \neq d_0$ and $t < l/v$

$$I = \sigma w v ln\left(\frac{l-vt}{l}\right) \tag{14b}$$

when $Rw\varepsilon_0 v = d_0$ and $t < l/v$

And the voltage output can be calculated by Ohm's law and is given by:

$$V = \sigma w v R\frac{d_0}{Rw\varepsilon_0 v - d_0}\left\{\frac{l}{l - vt}\exp\left[\frac{d_0}{Rw\varepsilon_0 v}\ln\left(\frac{l-vt}{l}\right)\right] - 1\right\} \tag{15a}$$

when $Rw\varepsilon_0 v \neq d_0$ and $t < l/v$

$$V = \sigma w v Rln\left(\frac{l-vt}{l}\right) \tag{15b}$$

Table 1. Parameters utilized in the FEM calculation and constant velocity theoretical calculation.

Dielectric 1	$\varepsilon_{r1} = 4$, $d_1 = 220$ μm
Dielectric 2	$\varepsilon_{r2} = 2$, $d_2 = 220$ μm
Width of Dielectrics w	0.1 m
Length of Dielectrics l	0.1 m
Tribo-charge surface density σ	7 μC m^{-2}
Maximum separation distance x_{max}	0.08 m
Velocity v	1 m/s

when $Rw\varepsilon_0 v = d_0$ and $t < l/v$

When R approaches to infinity, the general Equation (15a) can be simplified to Equation (7) to calculate V_{oc}. When R approaches to 0, the general Equation (13a) can be simplified to Equation (9) to calculate Q_{SC}. This also proves that the above results are correct.

The theoretical results for the model built for the FEM calculation at constant velocity moving mode is obtained through Equation (13) to Equation (15) by specifying the parameters, in the time range between 0 and x_{max}/v; when the time exceeds x_{max}/v, the in-plane charge separation stops and the current starts to decay exponentially (Section 3 in Supporting Information). These specified parameters are listed in **Table 1**, which is the same value as we used in the FEM calculation.

The x-t relationship for constant v is given by:

$$x = vt\left(t < \frac{x_{max}}{v}\right) \tag{16a}$$

$$x = x_{max}\left(t \geq \frac{x_{max}}{v}\right) \tag{16b}$$

Figure 4a shows the comparison of analytical calculation results of output current at R equals to 300 MΩ through Equation (14a) and semi-analytical model utilizing the data in Table S2 and Equation (12). The result of the two calculation gave the almost the same current output profile. Thus, the estimation by Equation (8) is accurate.

We calculated the profiles of Q, I and V at different loads utilizing the analytical model, as shown in Figure 4b–d. When the load resistance R is less than 1 MΩ, all of the curves are similar to the short-circuit curve that is given by Equation (9). The short-circuit charge Q_{SC} has a linear relationship with x and get its maximum when x reaches x_{max}. The driving force of this charge transfer is the electrostatic force from the tribo-charges. This driving force will provide an "expected" charge transfer rate from bottom electrode to top electrode. When the load resistance R is small, the real charge transfer rate can catch up with this "expected" charge transfer rate. Therefore, all of the curves are similar to the curves at the SC condition. Because of the constant speed we used in this calculation, when the top electrodes is still moving, the current is constant and proportional to the sliding speed of the top electrode. When load resistance R continues to increase, the shape of Q begins to deviate from the short-circuit curve. This is because the load resistance R limits the real charge transfer speed. Thus, the practical charge transfer speed cannot catch up with the "expected" charge transfer rate. The charge accumulation

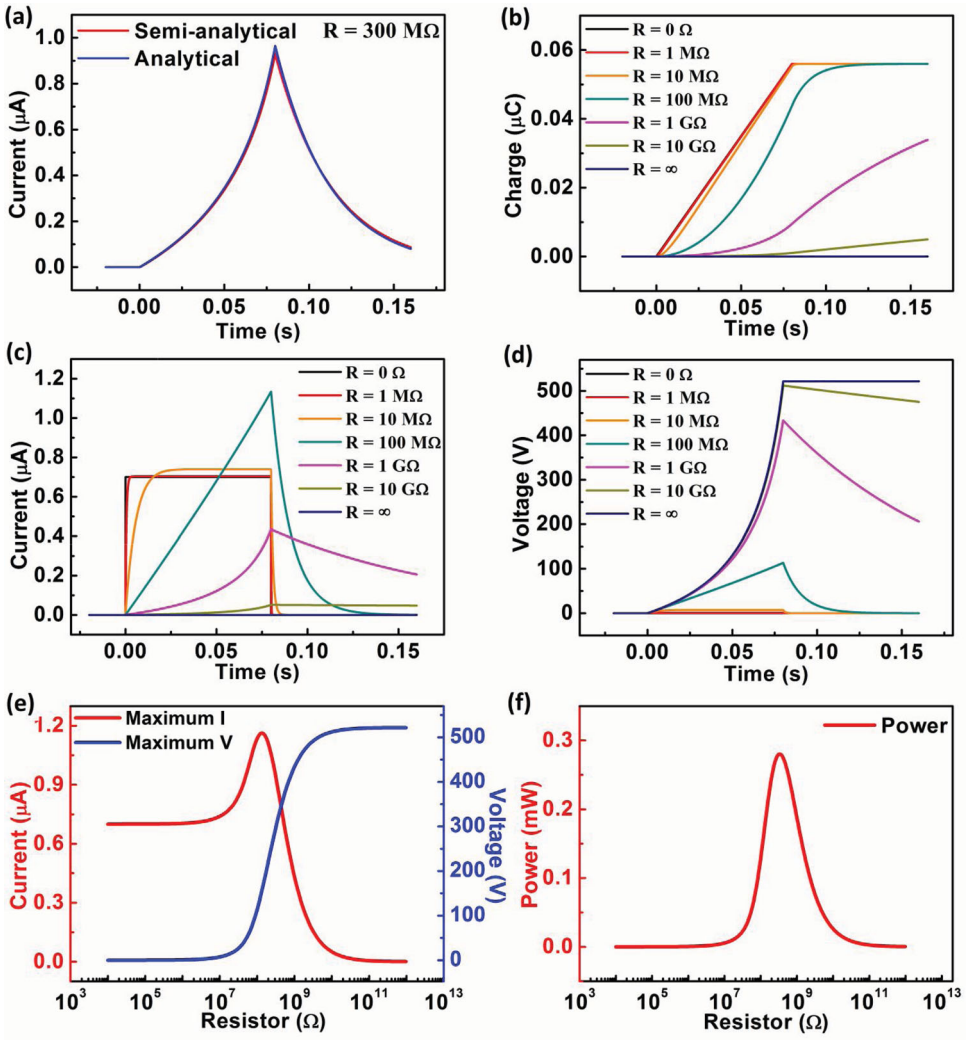

Figure 4. Theoretical calculation results for sliding under constant velocity. (a) Comparison of the current outputs calculated by semi-analytical interpolation equation and analytical equation with the external load of 300 MΩ. (b) Transferred charge-time relationship at different load resistances. (c) Current-time relationship at different load resistances. (d) Voltage-time relationship at different load resistances. (e) The influence of the load resistance on the maximum output current and voltage. (f) Maximum output power profile with load resistance.

process is slowed down and more time is needed for Q to get saturated. When load resistance is sufficiently high, very few charges can transfer from the bottom electrode. Therefore, the output performance is close to the open-circuit limit.

To better characterize the output performance of TENG change with the load resistance R, the peak values of current and voltage during this sliding process at different load resistances were extracted from Figure 4c and d and plotted in Figure 4e. The peak value of the output voltage is close to 0 when the load resistance is small. When the load resistance reaches about 10 MΩ, the output voltage begins to increase dramatically. When the load resistance reaches 10 GΩ, the output voltage is close to V_{OC} and gets saturated. The peak value of the output current has a different trend with that of the output voltage. When R is small, the peak value of the output current is close that of I_{SC}. When R increases, the peak value increases first, and then decreases to approximately 0 when R is sufficiently high. This increase is because that at this resistance region, the increasing speed of the voltage peak value is greater than the resistance increasing speed. The peak value of the power output is plotted in Figure 4f. An optimum resistance is observed for the instantaneous power output to reach its maximum, since either the output current or voltage will be close to zero at the high resistance or low resistance end, respectively. Moreover, the optimum resistance occurs at the region where output current and output voltage are dramatically changed.

To further verify the theoretical equation presented above, an experiment was designed to compare the experimental measurement results with the theoretical expectations. The experiment setup is shown in **Figure 5**a, similar to the experiment in our previous report.[11] The dielectrics we chose are Nylon and PTFE. Two metal electrodes were sputtered to one side of the polymer. Two glass slides were employed to support the whole structure. The bottom plate is fixed on the measurement platform and the top plate is driven by a linear motor. In the experiment, the motor was first accelerated and then decelerated with a

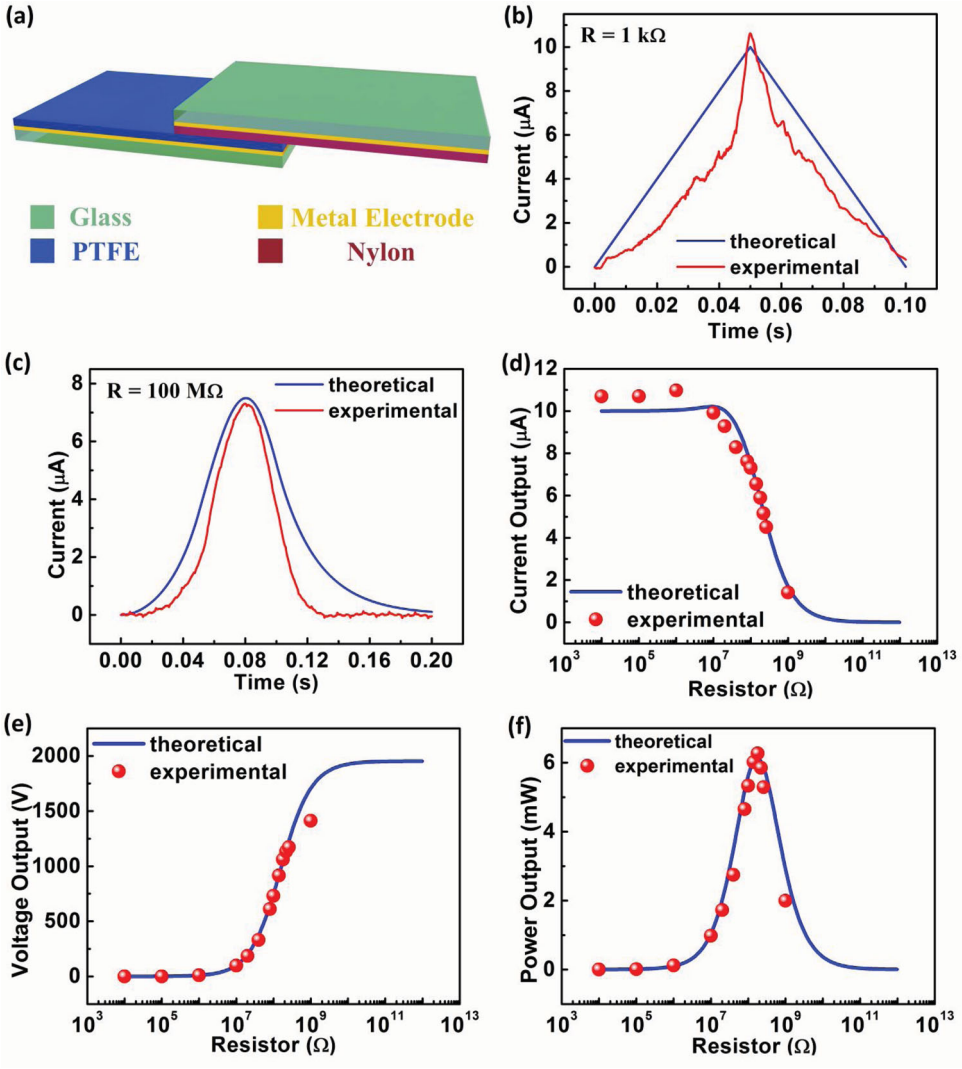

Figure 5. Theoretical calculation results of acceleration-deceleration model and the comparison with the corresponding experimental results (a) Device structure of the TENG used in the experiment. (b-c) Comparisons of current profiles from theoretical calculation and experiments at load resistances of (b) 1 kΩ and (c) 100 MΩ. (d-f) The theoretical influence of the load resistance on the maximum output (d) current, (e) voltage, and (f) power, with the comparison to the experimental results.

constant acceleration a. Therefore, in the theoretical calculation, the x-t relationship is given by the following equations.

$$x = \frac{1}{2}at^2 \left(t < \sqrt{\frac{x_{max}}{a}}\right) \tag{17a}$$

$$x = x_{max} - \frac{1}{2}a\left(2\sqrt{\frac{x_{max}}{a}} - t\right)^2 \left(\sqrt{\frac{x_{max}}{a}} \le t < 2\sqrt{\frac{x_{max}}{a}}\right) \tag{17b}$$

$$x = x_{max} \left(t \ge 2\sqrt{\frac{x_{max}}{a}}\right) \tag{17c}$$

The parameters used in the calculation and experiment are listed in **Table 2**.

The numerical theoretical prediction is calculated by utilizing the Equation (12) with x-t relationship given by the Equation (17). The theoretical results and corresponding experimental data are plotted in Figure 5b–f for comparison. Figure 5b and c show the current wave shape when R is 1 kΩ and 100 MΩ. The trend of the theoretical calculation matches the experimental data quite well. Furthermore, the theoretical and experimental peak values of current, voltage and power output are plotted in Figure 5d, e, and f. The

Table 2. Parameters utilized in the experiment and the acceleration-deceleration theoretical calculation.

Dielectric 1 Nylon	$\varepsilon_{r1} = 4$, $d_1 = 50$ μm
Dielectric 2 PTFE	$\varepsilon_{r2} = 2.1$, $d_2 = 50$ μm
Width of Dielectrics w	0.05 m
Length of Dielectrics l	0.071 m
Tribo-charge surface density σ	200 μC m^{-2}
Maximum separation distance x_{max}	0.05 m
Acceleration a	20 m/s^2

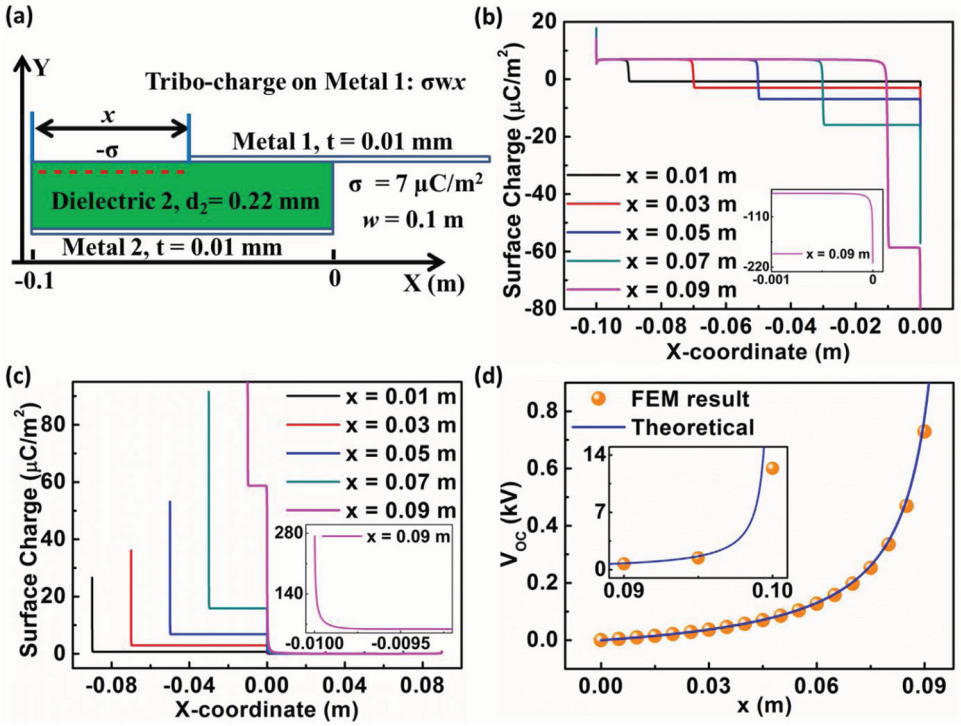

Figure 6. FEM calculation result of conductor-to-dielectric TENG at OC condition. (a) Structure of the FEM model. (b-c) Calculated charge distribution of (b) the upper face of the bottom electrode and (c) the lower face of the top electrode, the inset is the enlarged profile of the surface charge at the edges when x = 0.09 m. (d) Comparison of theoretical V_{OC}-x relationship with the values calculated by FEM, the inset is the profile of the V_{OC} when x approaches to l.

theoretical data and the experimental data show the same trend. The theoretical optimum resistance matches with the experimental result as well. This result again proves that our theoretical model is correct and can be utilized to estimate the experimental cases.

3. Conductor-to-Dielectric Sliding-Mode TENG

Besides the dielectric-to-dielectric sliding-mode TENG model, we derived the model for the conductor-to-dielectric case as well. The studied structure for this type of TENG is shown in **Figure 6**a. The only geometrical structure difference is the absence of Dielectric 1. In this case, Metal 1 is not only the top triboelectric layer, but also the top electrode itself. When Metal 1 and Dielectric 2 are separated, due to the triboelectric effect, the upper surface at the separated region of Dielectric 2 has the uniform tribo-charges (surface density is $-\sigma$) and the same amount of tribocharges with opposite sign will exist on the surface of Metal 1. Therefore, at the OC condition, the total amount of charges on the bottom electrode is 0. For the ease of simulation in FEM, the tribo-charges on the dielectric surface in the overlapped region has been deemed to cancel the opposite tribo-charge portions on the top metal layer, with the density of σ and amount of $w(l\text{-}x)\sigma$. Thus, in our FEM calculation, the total amount of charges on the top electrode is $wx\sigma$.

The model built in Figure 6a is calculated with COMSOL software at OC condition, which shows the similar charge distribution on the electrodes, as shown in Figure 6b and c. At each region, the charge distribution is still uniform. Similar to the above discussion and derivation, the ideal charge distribution can be given by:

For the non-overlapped region of the bottom electrode: $\rho = \sigma$ (18a)

For the overlapped region of the bottom electrode: $\rho = -\frac{\sigma x}{l - x}$ (18b)

For the non-overlapped region of the top electrode: $\rho = 0$ (18c)

For the overlapped region of the top electrode: $\rho = \frac{\sigma x}{l - x}$ (18d)

Utilizing the above charge distribution and Gauss Theorem, the electric field of the overlapped region in Dielectric 2 E_{y2} can be given by:

$$E_{y2} = \frac{\sigma x}{\varepsilon_0 \varepsilon_{r2} (l - x)} \quad (19)$$

Thus, the theoretical V_{OC} is given by:

$$V_{OC} = E_{y2} d_2 = \frac{\sigma x}{\varepsilon_0 (l - x)} \frac{d_2}{\varepsilon_{r2}} \quad (20)$$

The V_{OC} results from Equation (20) are compared with the FEM calculation results for the verification of the theoretical model, as shown in Figure 6d. When x is not close to l, the estimation by Equation (20) is very accurate.

Similarly, the capacitance C can be estimated by the parallel-plate capacitance at the overlapped region and is given by:

$$C = \frac{\varepsilon_0 \varepsilon_{r2} w (l - x)}{d_2} \tag{21}$$

Merge Equation (20) and (21) into Equation (2), the *V-Q-x* relationship for this type of TENG is given by:

$$V = -\frac{1}{w\varepsilon_0 (l - x)} \frac{d_2}{\varepsilon_{r2}} Q + \frac{\sigma x}{\varepsilon_0 (l - x)} \frac{d_2}{\varepsilon_{r2}} \tag{22}$$

Equation (22) is in the same form as Equation (8) when d_1 is set to 0. Therefore, all of the discussion in the dielectric-to-dielectric TENG applies to the conductor-to-dielectric TENG.

4. Conclusions

In summary, a theoretical model for the sliding-mode TENG is presented in this work. The finite element method has been utilized to characterize the distributions of electric potential, electric field, and charges on the metal electrodes of the TENG. Based on the FEM calculation, the semi-analytical results from the interpolation method and the analytical *V-Q-x* relationship were built to study the sliding-mode TENG. The analytical *V-Q-x* equation was validated through comparison with the semi-analytical results. Furthermore, based on the analytical *V-Q-x* equation, dynamic output performance of sliding-mode TENG was calculated with arbitrary load resistance, and good agreement with experimental data was reached. The theory presented here is a milestone work for in-depth understanding of the working mechanism of the sliding-mode TENG, and provides theoretical basis for further enhancement of the sliding-mode TENG for both energy scavenging and self-powered sensor applications.

Supporting Information

Supporting Information is available from the Wiley Online Library or from the author.

Acknowledgements

Research was supported by U.S. Department of Energy, Office of Basic Energy Sciences under Award DEFG02- 07ER46394, NSF, and the Knowledge Innovation Program of the Chinese Academy of Sciences (Grant KJCX2-YW-M13). S. Niu and Y. Liu contribute equally to this work.

Received: June 20, 2013
Revised: July 18, 2013
Published online: August 27, 2013

[1] B. Z. Tian, X. L. Zheng, T. J. Kempa, Y. Fang, N. F. Yu, G. H. Yu, J. L. Huang, C. M. Lieber, *Nature* **2007**, *449*, 885.
[2] M. S. Dresselhaus, G. Chen, M. Y. Tang, R. G. Yang, H. Lee, D. Z. Wang, Z. F. Ren, J. P. Fleurial, P. Gogna, *Adv. Mater.* **2007**, *19*, 1043.
[3] B. Oregan, M. Gratzel, *Nature* **1991**, *353*, 737.
[4] E. P. Murray, T. Tsai, S. A. Barnett, *Nature* **1999**, *400*, 649.
[5] Z. L. Wang, J. H. Song, *Science* **2006**, *312*, 242.
[6] S. P. Beeby, M. J. Tudor, N. M. White, *Meas. Sci. Technol.* **2006**, *17*, R175.
[7] C. E. Chang, V. H. Tran, J. B. Wang, Y. K. Fuh, L. W. Lin, *Nano Lett.* **2010**, *10*, 726.
[8] F. R. Fan, Z. Q. Tian, Z. L. Wang, *Nano Energy* **2012**, *1*, 328.
[9] F. R. Fan, L. Lin, G. Zhu, W. Z. Wu, R. Zhang, Z. L. Wang, *Nano Lett.* **2012**, *12*, 3109.
[10] S. H. Wang, L. Lin, Z. L. Wang, *Nano Lett.* **2012**, *12*, 6339.
[11] S. H. Wang, L. Lin, Y. N. Xie, Q. S. Jing, S. M. Niu, Z. L. Wang, *Nano Lett.* **2013**, *13*, 2226.
[12] G. Zhu, J. Chen, Y. Liu, P. Bai, Y. S. Zhou, Q. S. Jing, C. F. Pan, Z. L. Wang, *Nano Lett.* **2013**, *13*, 2282.
[13] L. Lin, S. H. Wang, Y. N. Xie, Q. S. Jing, S. M. Niu, Y. F. Hu, Z. L. Wang, *Nano Lett.* **2013**, *13*, 2916.
[14] R. G. Horn, D. T. Smith, *Science* **1992**, *256*, 362.
[15] R. G. Horn, D. T. Smith, A. Grabbe, *Nature* **1993**, *366*, 442.
[16] P. K. Watson, Z. Z. Yu, *J. Electrostat.* **1997**, *40–1*, 67.
[17] F. Saurenbach, D. Wollmann, B. D. Terris, A. F. Diaz, *Langmuir* **1992**, *8*, 1199.
[18] J. Stoer, R. Bulirsch, *Introduction to numerical analysis*, Springer, New York **2002**.